chemical physics program through the Chemical Sciences Division of Lawrence Berkeley National Laboratory (LBNL). K.S. gratefully acknowledges financial support from the Volkswagen Foundation. The apparatus was partially funded by the NSF Engineering Research Center for Extreme Ultraviolet Science and Technology, under a previously completed grant (no. EEC-0310717). Theoretical work by C.D.P, K.D.C, and D.P was performed as part of a User Project at The Molecular Foundry (TMF), LBNL. TMF is supported by the Office of Science, Office of Basic Energy Sciences, of the U.S. DOE, under contract no. DE-AC02-05CH11231. Portions of C.D.P's work integrating nonadiabatic dynamics into transient x-ray absorption spectral simulations were carried out within the Theory Institute for Materials and Energy Spectroscopies at SLAC, supported by the U.S. DOE, Office of Basic Energy Sciences, Division of Materials Sciences and Engineering, under contract no. DE-AC02-76SF00515. Numerical simulations were executed on the Vulcan, Mako, and Lawrencium compute clusters, administered by the High-Performance Computing Services Group at LBNL. All data in both the main manuscript and supplementary materials will be made available upon request.

SUPPLEMENTARY MATERIALS

www.sciencemag.org/content/356/6333/54/suppl/DC1
Materials and Methods
Supplementary Text
Figs. S1 to S17
References (*34–64*)

18 September 2016; resubmitted 24 January 2017
Accepted 22 February 2017
10.1126/science.aaj2198

SOLAR CELLS

Long-range hot-carrier transport in hybrid perovskites visualized by ultrafast microscopy

Zhi Guo,[1] Yan Wan,[1] Mengjin Yang,[2] Jordan Snaider,[1] Kai Zhu,[2] Libai Huang[1]*

The Shockley-Queisser limit for solar cell efficiency can be overcome if hot carriers can be harvested before they thermalize. Recently, carrier cooling time up to 100 picoseconds was observed in hybrid perovskites, but it is unclear whether these long-lived hot carriers can migrate long distance for efficient collection. We report direct visualization of hot-carrier migration in methylammonium lead iodide ($CH_3NH_3PbI_3$) thin films by ultrafast transient absorption microscopy, demonstrating three distinct transport regimes. Quasiballistic transport was observed to correlate with excess kinetic energy, resulting in up to 230 nanometers transport distance that could overcome grain boundaries. The nonequilibrium transport persisted over tens of picoseconds and ~600 nanometers before reaching the diffusive transport limit. These results suggest potential applications of hot-carrier devices based on hybrid perovskites.

Hot (nonequilibrium) carrier thermalization is one of the major sources for efficiency loss in solar cells (*1*). Such loss can be reverted if the hot carriers can be harvested before they equilibrate with the lattice, and the ultimate thermodynamic limit on conversion efficiency can be increased from the Shockley-Queisser limit of 33% to about 66% (*1*, *2*). The main challenge for harvesting hot carriers is the relatively short distance they travel before losing their excess energy to the lattice, typically on the picosecond time scale (*3–8*). Hybrid organic-inorganic metal halide perovskites, such as $CH_3NH_3PbI_3$, have emerged to be a class of highly efficient solar cell materials with remarkable charge transport properties, achieving efficiency above 20% (*9–13*). Recently, ultrafast spectroscopic measurements have revealed surprisingly long-lived hot carriers on the order of 100 ps in these hybrid perovskites (*14–18*).

The remarkably long hot-carrier lifetime in the hybrid perovskites, about two to three orders of magnitude longer than in conventional semiconductors, raises the question of whether hot carriers can be harvested to overcome the Shockley-Queisser limit. However, the current understanding on hot-carrier transport in hybrid perovskites is limited, despite efforts that have been devoted to studying carrier cooling dynamics (*14–21*). In particular, the crucial parameter of hot-carrier transport length must be comparable to the thickness necessary for photon absorbance.

To correctly evaluate the potential of hot-carrier perovskite solar cells, measurements to provide quantitative results on the length scales of hot-carrier transport in relation to carrier cooling time scales are necessary. Combining microscopy techniques with ultrafast optical pumping can be an effective solution for achieving simultaneous temporal and spatial resolutions of carrier dynamics (*22–25*). Here, we report on a direct visualization of hot-carrier transport in $CH_3NH_3PbI_3$ thin films using ultrafast transient absorption microscopy (TAM) with 50-nm spatial precision and 300-fs temporal resolution. These experiments revealed three distinct transport regimes, specifically, quasiballistic transport for the initial hot carriers, nonequilibrium transport for the protected long-lived hot carriers, and diffusive transport for the cooled carriers.

We performed measurements on a uniform and highly crystalline $CH_3NH_3PbI_3$ perovskite thin film deposited on a SiO_2 substrate, and a scanning electron microscopy (SEM) image is shown in fig. S1 of the supplementary materials (SM) (*26*). Solar cell efficiencies of ~18% have been achieved by using films fabricated with the same procedure (*27*). The absorption and photoluminescence spectra of the thin film investigated are shown in fig. S2 (*26*).

We first carried out ensemble transient absorption measurements to establish spectroscopic signatures for hot carriers (Fig. 1). Immediately after photoexcitation, a photoinduced absorption (PIA, negative change of transmission $\Delta T/T$) band centered at 1.58 eV was observed whose amplitude ($|\Delta T/T|$) increased as the pump photon energy increased (Fig. 1A). Global analysis (Fig. 1B) indicates that this PIA band is associated with a broadened ground-state bleach (GSB, positive $\Delta T/T$) band with a high-energy tail consistent with Fermi-Dirac distribution at high carrier temperature. The PIA band resulted from the shifting of the band-gap energy ΔE_g, which was a combination of band-gap renormalization effect (narrowing the band gap by ΔE_{BGN}) and Burstein-Moss effect (or band-filling, widening the band gap by ΔE_{BM}), as described by $\Delta E_g = \Delta E_{BM} - \Delta E_{BGN}$ (*28*). Because ΔE_{BM} would not take effect until the hot carriers relax to the band edge, the red-shifted PIA band at 1.58 eV at 0 ps was due to ΔE_{BGN} predominantly. The amplitude of the PIA band increased as the pump photon energy increased, which could be explained by the decreased occupation of the states near the band edge leading to a decreased ΔE_{BM}. Once carriers cooled down and ΔE_{BM} settled in, the PIA band at 1.58 eV decayed and a blue-shifted PIA band was observed (fig. S3) (*26*). Based on these observations, we assigned the PIA band at 1.58 eV to hot carriers, in agreement with previous reports (*29*, *30*).

$\Delta T/T$ of the PIA band had a different dependence on carrier density n than that of the GSB band when probed at 1.58 eV (Fig. 1C). $\Delta T/T$ of the GSB band scaled linearly with n, whereas $\Delta T/T$ of the PIA band was proportional to $n^{1/2}$. Because $\Delta T/T$ of the PIA band scaled linearly with ΔE_{BGN} as empirically shown in (*14*), this observation indicated that $\Delta E_{BGN} \propto n^{1/2}$. A $n^{1/3}$ dependence for ΔE_{BGN} is generally expected when carriers are weakly interacting, but an $n^{1/2}$ term must be included when carrier-carrier interactions become more important (*28*, *31*). For instance, the $n^{1/2}$ dependence becomes dominant at $n > 10^{17}$ cm^{-3} for GaAs (*31*). The $n^{1/2}$ dependence observed here implies that carrier-carrier interactions are not negligible for $CH_3NH_3PbI_3$.

The PIA band decayed with a ~400-fs time constant when excited at 3.14 eV (Fig. 1B), which has been assigned to the emission of the longitudinal optical phonons (*14*, *21*, *32*). The lifetime for the PIA band shortened to ~280 fs when the pump photon energy was reduced to 1.97 eV (fig. S4) (*26*). The decay of the PIA band was

[1]Department of Chemistry, Purdue University, West Lafayette, IN 47907, USA. [2]National Renewable Energy Laboratory, 15013 Denver West Parkway, Golden, CO 80401, USA.
*Corresponding author. Email: libai-huang@purdue.edu

accompanied by the growth of the GSB band at the band edge (Fig. 1D). Also shown in Fig. 1D is a second and slower cooling process with a time constant of ~78 ps. The much slower cooling phase has been ascribed to the protection of the energetic carriers by the formation of large polarons (*15*, *16*), hot phonon effects (carrier density > 10^{18} cm^{-3}) (*14*), and optical-acoustic phonon scattering (*17*).

We imaged hot-carrier transport initiated by two different pump photon energies: 3.14 eV (1.49 eV above band gap) and 1.97 eV (0. 32 eV above band gap) with a probe photon energy of 1.58 eV. The pump beam was held at a fixed position while the probe beam was scanned relative to the pump with a pair of galvanometer scanners to form an image (see more details in the SM, fig. S5) (*23*, *26*, *33*). The precision in determining carrier propagation distance was dictated by the smallest measurable change in the excited state population profiles and not directly by the diffraction limit (*34*). This limit is ~50 nm for the current experimental conditions, as discussed in the SM (*26*). The carrier density for these measurements was ~4×10^{17} cm^{-3}, where Auger recombination and hot phonon effect were negligible (fig. S6) (*16*, *26*, *33*).

The initial population was created by a Gaussian pump beam at position (x_0, y_0), with a pulse duration of ~300 fs. We defined an instrument response function (IRF) = $\sqrt{\sigma^2(pump) + \sigma^2(probe)}$ that described the response of a pump-probe microscope to a point object, where $\sigma^2(pump)$ and $\sigma^2(probe)$ were the variance of the Gaussian pump and probe beams. The IRF was determined to be 260 ± 5 nm (Fig. 2C) by measuring a tetracene single crystal under similar experimental conditions at 0 ps because exciton transport within the pulse width for tetracene is negligible (*23*).

At 0-ps time delay, carrier distribution should be equal to the convolution of the probe and probe beams if no transport occurs within the pulse width. Only negative ΔT (PIA) was observed at 0-ps delay, indicating that the initially created carriers were out of equilibrium for both pump photon energies. Because the ΔT_{PIA} is proportional to $n^{1/2}$, the carrier distribution can be obtained by $n(x, y, 0) \propto [\Delta T_{PIA}(x, y, 0)]^2$. For 3.14 eV photon excitation, the 0-ps image showed morphology-dependent structures that were not easily described by a Gaussian function (Fig. 2A). To average out the morphological effects, we interpolated $[\Delta T_{PIA}(x, y, 0)]^2$ onto a polar coordinate, summed over all angles, and plotted it as a function of radial distance (Fig. 2C). Carrier distribution at 0 ps was fitted by a Gaussian function with a variance σ_0^2 of 350 ± 10 nm, much larger than that of the IRF (Fig. 2C). Thus, hot-carrier transport must have occurred within the pulse duration. The transport distance within the pulse width was calculated as $\sqrt{\sigma_0^2 - IRF^2}$ = 230 ± 16 nm. In contrast, when the pump photon energy was reduced to 1.97 eV (Fig. 2B), negligible carrier transport within the pulse width was observed and the initial hot-carrier population distribution was similar to the IRF (fig. S7) (*26*).

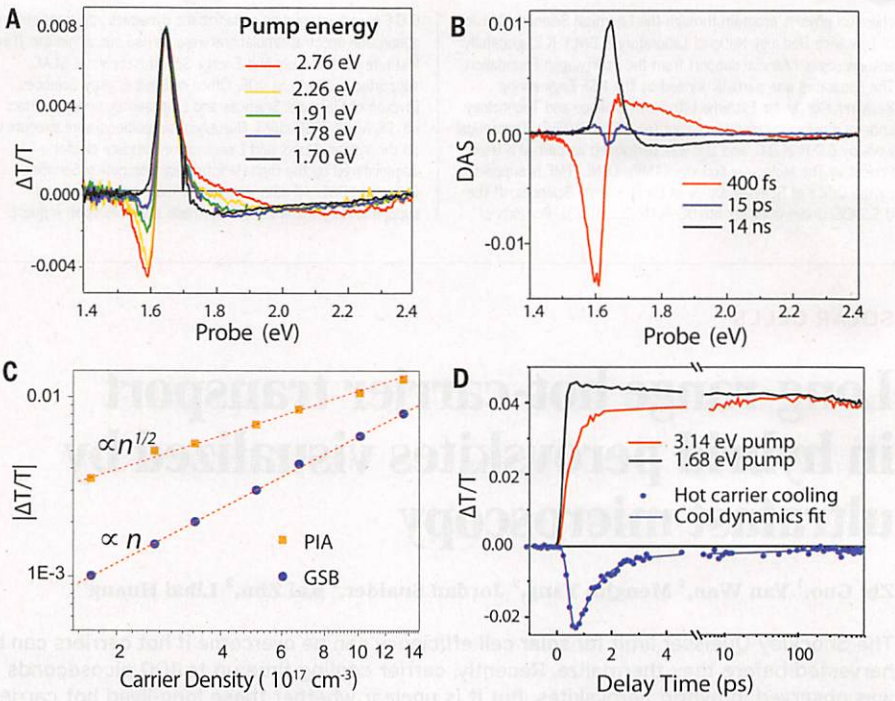

Fig. 1. Spectral signatures of the hot carriers. (**A**) Ensemble transient absorption spectra taken at 200-fs delay with different pump photon energies and change of transmission $\Delta T/T$ was plotted. The pump fluences were calibrated to the same carrier density of 10^{17} cm^{-3}. (**B**) Decay-associated spectra (DAS) for a pump photon energy of 3.14 eV obtained by performing global analysis on the transient spectra. (**C**) Carrier density dependence of $\Delta T/T$ of the PIA band (taken at maximum value) and that of the GSB band (taken at 4-ps time delay) for a pump photon energy of 3.14 eV and a probe energy of 1.58 eV. (**D**) Hot-carrier cooling kinetics obtained by subtracting the carrier relaxation kinetics driven by 3.14-eV photon excitation from those induced by 1.68-eV excitation plotted along with a biexponential fit.

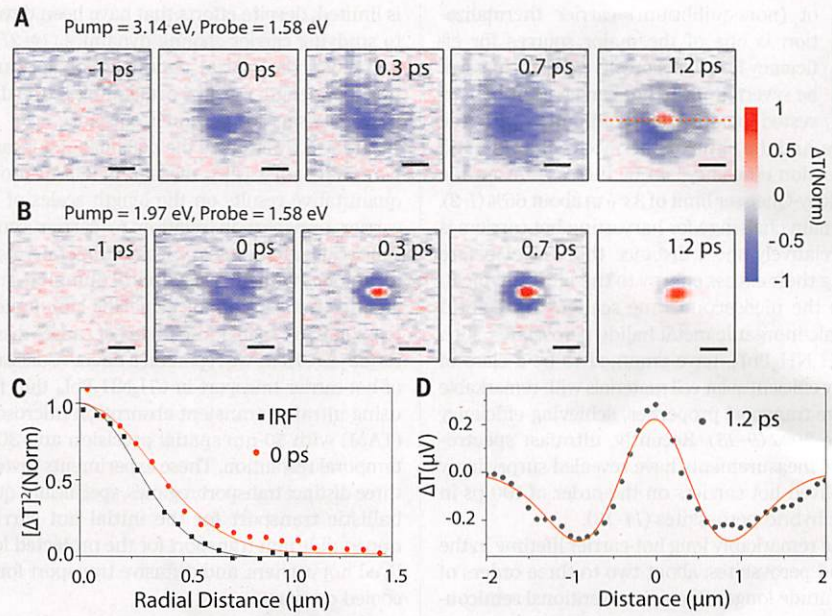

Fig. 2. Hot-carrier transport within the first picosecond. TAM images probing at 1.58 eV with two pump photon energies—(**A**) 3.14 eV and (**B**) 1.97 eV—at different pump-probe delay times, as labeled. Scale bars, 1 μm. (**C**) Hot-carrier distribution at 0-ps delay for 3.14-eV excitation over a radial distance obtained by averaging all angles compared to the IRF, as defined in the text. Solid lines are Gaussian fits. (**D**) One-dimensional TAM image profile at 1.2 ps for 3.14-eV pump excitation. The red solid line is fit as described in the text. The red dashed line in (A) indicates where the 1D distribution was obtained in (D).

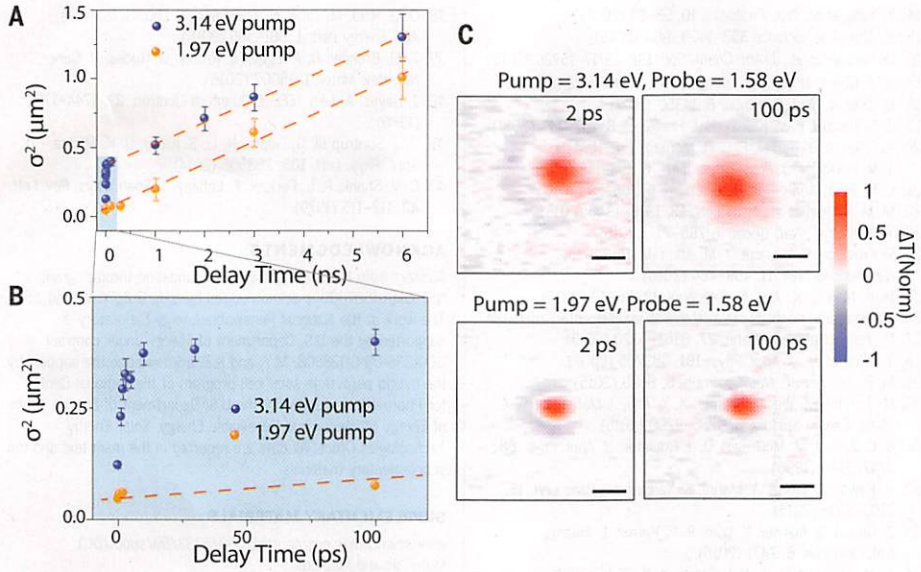

Fig. 3. Nonequilibrium to diffusive transport transition. (**A**) σ_t^2 plotted as a function of pump-probe delay time up to 6 ns for 1.97-eV and 3.14-eV pump photon energies. Linear fits are shown in dashed red lines to indicate diffusive transport. (**B**) Zoomed-in view of (A) for the first 100 ps pump-probe delay. (**C**) TAM images at 2 ps and 100 ps for 3.14-eV and 1.97-eV pump photon energies. Scale bars, 1 μm.

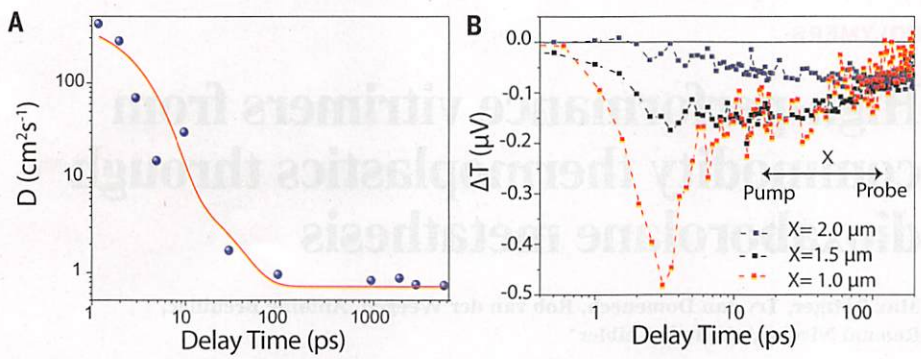

Fig. 4. Time dependence of carrier transport. (**A**) Effective diffusion constant calculated as $D(t)$ as a function of delay time for 3.14-eV photon excitation. The red solid line is the fit to a biexponential decay function. (**B**) Kinetics probed at pump-probe distances as labeled for pump photon energy of 3.14 eV.

The excess energy-dependent carrier transport distance within the pulse width indicated that ballistic carrier transport played a role. When promoting carriers from the valance band to the conduction band, the excess energy above the band gap manifested as kinetic energy and distributed among the electrons and holes inversely proportional to their respective effective masses, m_e^* and m_h^* (*2*), which for $CH_3NH_3PbI_3$ both have a value of ~0.2 m_0, the free electron mass (*35*, *36*). The ballistic velocity of the carriers v_{max} is given by $K_{e(h)} = \frac{1}{2} m_{e(h)}^* v_{max}^2$, leading to a value of 1.6×10^6 and 0.7×10^6 ms^{-1} for 3.14 eV and 1.97 pump photon energies, respectively. For 3.14 eV excitation, the expansion of the width of the TAM image within the pulse width gave a velocity of 230 nm/300 fs = 0.8×10^6 ms^{-1}, on the same order as v_{max}, indicating that the carrier motion was quasiballistic. Our time resolution was unable to resolve ballistic transport directly. Intriguingly, very little quasiballistic transport was observed for 1.97 eV excitation, which was probably limited by grain boundaries. There could be additional potential barriers at interfaces or "dynamic" barriers created by the fluctuating energy landscape that could also require excess kinetic energy to overcome (*37*). The larger initial kinetic energies of the hot carriers created by 3.14 eV pump allowed more carriers to overcome grain boundaries, as shown in the 0-ps image in Fig. 2A.

Carrier cooling was also visualized by TAM, manifested as the negative ΔT signal (PIA) turning into the positive ΔT signal (GSB). The GSB signal appeared sooner for the 1.97 eV pump (after 300 fs) than for the 3.14 eV pump (after 1 ps), consistent with less excess energy to lose to the phonons. The GSB signal presented initially only in the center of TAM images, which can be explained by the PIA and the GSB ΔT having opposite signs and different carrier density dependence—i.e., $\Delta T_{PIA}(x,y,t) \propto -n(x,y,t)^{1/2}$ and $\Delta T_{GSB}(x,y,t) \propto n(x,y,t)$. The TAM profiles were then fitted using two-dimensional (2D) Gaussian functions for $n(x,y,t)$, with variances of $\sigma_{x,t}^2$ and $\sigma_{y,t}^2$ as detailed in the SM (*26*). Fits along one dimension for 1.2-ps pump-probe delay is shown in Fig. 2D (data for 100-ps delay shown in fig. S8) (*26*). Because the carrier transport was isotropic—i.e., $\sigma_{x,t}^2 \approx \sigma_{y,t}^2$, we reduced the problem to 1D and defined $\sigma_t^2 = \frac{\sigma_{x,t}^2 + \sigma_{y,t}^2}{2}$ to average out morphological effects and plotted it as a function of pump-probe delay time in Fig. 3, A and B.

Carriers continued to move more rapidly for 3.14 eV excitation than 1.97 eV excitation on the 10s of picosecond time scale (Fig. 3, B and C), as the second and slower phase of carrier cooling set in (*15*–*17*). For 1.97 eV pump, σ_t^2 grew linearly as a function of delay time for > 1 ps, indicative of diffusive transport as described by $\sigma_t^2 - \sigma_0^2 = 2Dt$ (D is the diffusion coefficient, 0.7 ± 0.1 cm^2 s^{-1}) (*34*). This large D value is consistent with the high crystallinity of our sample (*38*). Diffusive transport indicated that thermal equilibrium with the lattice was reached. However, for the 3.14-eV excitation, diffusive transport was not observed until after 30 ps, and hot carriers migrated ~600 nm before reaching thermal equilibrium with the lattice. The diffusion coefficient was identical for 3.14-eV and 1.97-eV excitation after 100 ps. Recently, Li *et. al.* (*18*) estimated almost an order of magnitude shorter hot-carrier transport distance of 16 to 90 nm for films of $CH_3NH_3PbBr_3$ nanoparticles, despite the fact that hot-carrier cooling times were two orders of magnitude slower in these nanoparticles than in bulk films. Thus, our results suggest that slow carrier cooling alone does not necessary lead to long-range transport, and morphology is also a critical factor.

We calculated the effective diffusion constant as $D(t) = \frac{\Delta\sigma_t^2(t)}{2\Delta t}$ for the 3.14-eV excitation. $D(t)$ decreased from an initial value of 450 ± 10 cm^2 s^{-1} at 1 ps to the equilibrium value of 0.7 ± 0.1 cm^2 s^{-1} and could be fitted to a biexponential decay function with decay constants of 3 ± 1 ps and 20 ± 5 ps, respectively (Fig. 4A). The decay-time constants agreed overall with carrier cooling time. The fast decay-time constant (3 ps) was slower than that determined from the ensemble transient absorption measurements (400 fs), which can be understood as that the ensemble measurements integrating over a large area underestimated the cooling time because the PIA and GSB signals canceled each other out. Time-dependent carrier transport behavior was also observed directly in the corresponding carrier dynamics when probing away from the pump beam center with a 3.14-eV pump (Fig. 4B). The rapid growth of hot-carrier population (negative ΔT signal) when probing 1 μm and 1.5 μm away from the pump center persisted up to ~3 ps in good agreement with the initial fast transport, and the growth slowed down on the 10s of picosecond time scale. The fast growth was absent when probing 2 μm away because the initial fast transport did not reach that distance.

To understand the factors contributing to the extraordinary long-range hot-carrier transport, we compared $CH_3NH_3PbI_3$ to other conventional

inorganic semiconductors. $CH_3NH_3PbI_3$ has comparable electron effective mass as Si (*39*), and the ballistic velocity on the order of 10^6 ms^{-1} is also consistent with recent calculation for Si (*6*). The quasiballistic transport length of ~230 nm in 300 fs for $CH_3NH_3PbI_3$, however, is much longer than that of ~85 nm for GaAs (*40*), ~20 nm for Si (*6*), and ~14 nm for GaN (*41*) and can be explained by slower momentum relaxation in $CH_3NH_3PbI_3$ than in conventional semiconductors, ~100 fs as predicted by first principle calculations for hot carriers with excess energy of 1 eV (*32*). In comparison, relaxation times of 10 to 20 fs were found for hot carriers with excess energy > 0.3 eV for Si (*6*).

The nonequilibrium transport behavior of carriers in $CH_3NH_3PbI_3$ over 10s of picoseconds also deviates from conventional semiconductors such as Si and GaAs, for which equilibrium with the lattice is achieved in a few picoseconds (*5*, *42*). Interestingly, nonequilibrium carrier transport on the picosecond time scale was not observed when pump photon energy is reduced to 1.97 eV. An energetic E^* state with an energy of ~0.3 eV above the band edge has been observed to form at ~1 ps by two-photon photon emission spectroscopy and is also confirmed by density-of-state calculation (*15*, *16*). This E^* state probably could not be created by 1.97 eV (0.32 eV above band edge) photon excitation because of insufficient excess energy. Based on these observations, we attributed the nonequilibrium transport over 10s of picoseconds to hot carriers associated with the energetic E^* state. The E^* state is accompanied by the formation of large polarons occurring on the ~1-ps time scale (*16*). The long-lived and nondiffusive transport observed is also consistent with the large polaron picture, because the slow decay constant for D agrees well with the slow cooling of hot polarons by acoustic phonon scattering (*16*). These polarons are "heavier" than the bare carriers with nonparabolic dispersion (*37*), which could explain a lower diffusion coefficient on the 10s of picosecond time scale. The long-range hot-carrier transport is most likely not limited to $CH_3NH_3PbI_3$, because many hybrid organic-inorganic metal halide perovskites share similar carrier relaxation characteristics. The long-range motion associated with slow carrier cooling processes makes hybrid perovskites potential materials for hot-carrier devices.

REFERENCES AND NOTES

1. R. T. Ross, A. J. Nozik, *J. Appl. Phys.* **53**, 3813–3818 (1982).
2. A. J. Nozik, *Annu. Rev. Phys. Chem.* **52**, 193–231 (2001).
3. L. Reggiani, Ed., *Hot-Electron Transport in Semiconductors* (Springer Berlin Heidelberg, 1985), vol. 58.
4. J. Shah, *IEEE J. Quantum Electron.* **22**, 1728–1743 (1986).
5. B. B. Hu *et al.*, *Phys. Rev. Lett.* **74**, 1689–1692 (1995).
6. M. Bernardi, D. Vigil-Fowler, J. Lischner, J. B. Neaton, S. G. Louie, *Phys. Rev. Lett.* **112**, 257402 (2014).
7. M. Bernardi, D. Vigil-Fowler, C. S. Ong, J. B. Neaton, S. G. Louie, *Proc. Natl. Acad. Sci. U.S.A.* **112**, 5291–5296 (2015).
8. D. Lock, K. R. Rusimova, T. L. Pan, R. E. Palmer, P. A. Sloan, *Nat. Commun.* **6**, 8365 (2015).
9. M. M. Lee, J. Teuscher, T. Miyasaka, T. N. Murakami, H. J. Snaith, *Science* **338**, 643–647 (2012).
10. J. Burschka *et al.*, *Nature* **499**, 316–319 (2013).
11. Q. Dong *et al.*, *Science* **347**, 967–970 (2015).
12. W. Nie *et al.*, *Science* **347**, 522–525 (2015).
13. G. Xing *et al.*, *Science* **342**, 344–347 (2013).
14. Y. Yang *et al.*, *Nat. Photonics* **10**, 53–59 (2016).
15. H. Zhu *et al.*, *Science* **353**, 1409–1413 (2016).
16. D. Niesner *et al.*, *J. Am. Chem. Soc.* **138**, 15717–15726 (2016).
17. A. Y. Chang *et al.*, *Adv. Energy Mater.* **6**, 1600422 (2016).
18. M. Li *et al.*, *Nat. Commun.* **8**, 14350 (2017).
19. J. S. Manser, P. V. Kamat, *Nat. Photonics* **8**, 737–743 (2014).
20. K. Chen, A. J. Barker, F. L. C. Morgan, J. E. Halpert, J. M. Hodgkiss, *J. Phys. Chem. Lett.* **6**, 153–158 (2015).
21. L. M. Herz, *Annu. Rev. Phys. Chem.* **67**, 65–89 (2016).
22. M. M. Gabriel *et al.*, *Nano Lett.* **13**, 1336–1340 (2013).
23. Y. Wan *et al.*, *Nat. Chem.* **7**, 785–792 (2015).
24. V. Kravtsov, R. Ulbricht, J. M. Atkin, M. B. Raschke, *Nat. Nanotechnol.* **11**, 459–464 (2016).
25. M. K. Man *et al.*, *Nat. Nanotechnol.* **12**, 36–40 (2017).
26. Materials and methods are available as supplementary materials.
27. M. Yang *et al.*, *Adv. Mater.* **27**, 6363–6370 (2015).
28. J. G. Lu *et al.*, *J. Appl. Phys.* **101**, 083705 (2007).
29. M. B. Price *et al.*, *Nat. Commun.* **6**, 8420 (2015).
30. M. T. Trinh, X. Wu, D. Niesner, X. Y. Zhu, *J. Mater. Chem. A Mater. Energy Sustain.* **3**, 9285–9290 (2015).
31. S. C. Jain, J. M. McGregor, D. J. Roulston, *J. Appl. Phys.* **68**, 3747–3749 (1990).
32. H. Kawai, G. Giorgi, A. Marini, K. Yamashita, *Nano Lett.* **15**, 3103–3108 (2015).
33. Z. Guo, J. S. Manser, Y. Wan, P. V. Kamat, L. Huang, *Nat. Commun.* **6**, 7471 (2015).
34. G. M. Akselrod *et al.*, *Nat. Commun.* **5**, 3646 (2014).
35. E. Menéndez-Proupin, P. Palacios, P. Wahnón, J. C. Conesa, *Phys. Rev. B* **90**, 045207 (2014).
36. A. Miyata *et al.*, *Nat. Phys.* **11**, 582–587 (2015).
37. Y. Chen *et al.*, *Nat. Commun.* **7**, 12253 (2016).
38. O. G. Reid, M. Yang, N. Kopidakis, K. Zhu, G. Rumbles, *ACS Energy Lett.* **1**, 561–565 (2016).
39. T. M. Brenner, D. A. Egger, L. Kronik, G. Hodes, D. Cahen, *Nat. Rev. Mater.* **1**, 15007 (2016).
40. J. Hayes, A. Levi, *IEEE J. Quantum Electron.* **22**, 1744–1752 (1986).
41. D. J. Suntrup III, G. Gupta, H. Li, S. Keller, U. K. Mishra, *Appl. Phys. Lett.* **105**, 263506 (2014).
42. C. V. Shank, R. L. Fork, R. F. Leheny, J. Shah, *Phys. Rev. Lett.* **42**, 112–115 (1979).

ACKNOWLEDGMENTS

Support from the National Science Foundation through grant NSF-DMR-1507803 is acknowledged by L.H., G.Z., Y.W., and J.S. The work at the National Renewable Energy Laboratory is supported by the U.S. Department of Energy under contract DE-AC36-08-GO28308. M.Y. and K.Z. acknowledge the support by the hybrid perovskite solar cell program of the National Center for Photovoltaics funded by the U.S. Department of Energy, Office of Energy Efficiency and Renewable Energy, Solar Energy Technologies Office. All data are reported in the main text and the supplementary materials.

SUPPLEMENTARY MATERIALS

www.sciencemag.org/content/356/6333/59/suppl/DC1
Materials and Methods
Figs. S1 to S8
References (*43*, *44*)

16 January 2017; accepted 2 March 2017
10.1126/science.aam7744

POLYMERS

High-performance vitrimers from commodity thermoplastics through dioxaborolane metathesis

Max Röttger, Trystan Domenech, Rob van der Weegen, Antoine Breuillac, Renaud Nicolaÿ,* Ludwik Leibler*

Windmills, cars, and dental restoration demand polymer materials and composites that are easy to process, assemble, and recycle while exhibiting outstanding mechanical, thermal, and chemical resistance. Vitrimers, which are polymer networks able to shuffle chemical bonds through exchange reactions, could address these demands if they were prepared from existing plastics and processed with fast production rates and current equipment. We report the metathesis of dioxaborolanes, which is rapid and thermally robust, and use it to prepare vitrimers from polymers as different as poly(methyl methacrylate), polystyrene, and high-density polyethylene that, although permanently cross-linked, can be processed multiple times by means of extrusion or injection molding. They show superior chemical resistance and dimensional stability and can be efficiently assembled. The strategy is applicable to polymers with backbones made of carbon-carbon single bonds.

Thermoplastics are light, tough, and easy to process but are limited by their lower strength, structural stability at high temperature, abrasion, and solvent resistances. Cross-linking could be the solution to improve these properties but reduces the ability of thermoplastics to flow when heated. As a result, the synthesis, processing, and recycling of cross-linked polymers, called thermosets, are complex and costly, if not impossible. Environmental awareness and industrial competitiveness cripple the introduction and development of cross-linked polymer materials.

Vitrimers (*1*, *2*) behave like permanently cross-linked materials at service temperatures, are insoluble at all temperatures, but can still flow when heated. Vitrimers consist of a polymer network that is able to change its topology without

Matière Molle et Chimie, École Supérieure de Physique et de Chimie Industrielles de la Ville de Paris (ESPCI)–CNRS, UMR-7167, Paris Sciences et Lettres (PSL) Research University, 10 Rue Vauquelin, 75005 Paris, France.
***Corresponding author. Email: renaud.nicolay@espci.fr (R.N.); ludwik.leibler@espci.fr (L.L.)**